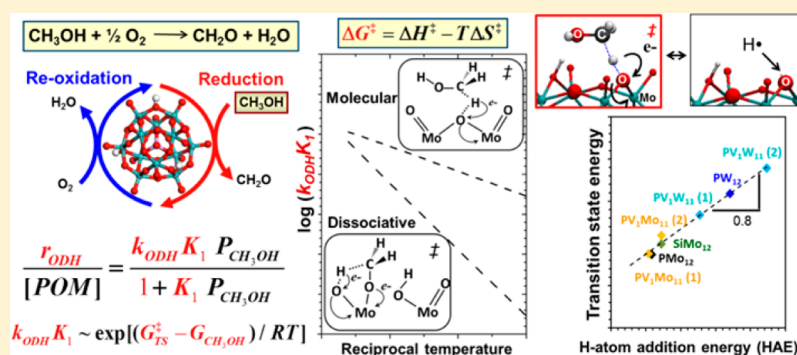


Methanol Oxidative Dehydrogenation on Oxide Catalysts: Molecular and Dissociative Routes and Hydrogen Addition Energies as Descriptors of Reactivity

Prashant Deshlahra[†] and Enrique Iglesia^{*,†,‡}[†]Department of Chemical Engineering, University of California at Berkeley, Berkeley, California 94720, United States[‡]Chemical Sciences Division, E.O. Lawrence Berkeley National Laboratory, Berkeley, California 94720, United States**S** Supporting Information

ABSTRACT: The oxidative dehydrogenation (ODH) of alkanols on oxide catalysts is generally described as involving H-abstraction from alkoxy species formed via O–H dissociation. Kinetic and isotopic data cannot discern between such routes and those involving kinetically-relevant H-abstraction from undissociated alkanols. Here, we combine such experiments with theoretical estimates of activation energies and entropies to show that the latter molecular routes prevail over dissociative routes for methanol reactions on polyoxometalate (POM) clusters at all practical reaction temperatures. The stability of the late transition states that mediate H-abstraction depend predominantly on the stability of the O–H bond formed, making H-addition energies (HAE) accurate and single-valued descriptors of reactivity. Density functional theory-derived activation energies depend linearly on HAE values at each O-atom location on clusters with a range of composition ($\text{H}_3\text{PMo}_{12}$, $\text{H}_4\text{SiMo}_{12}$, H_3PW_{12} , $\text{H}_4\text{PV}_1\text{Mo}_{11}$, and $\text{H}_4\text{PV}_1\text{W}_{11}$); both barriers and HAE values reflect the lowest unoccupied molecular orbital energy of metal centers that accept the electron and the protonation energy of O-atoms that accept the proton involved in the H-atom transfer. Bridging O-atoms form O–H bonds that are stronger than those of terminal atoms and therefore exhibit more negative HAE values and higher ODH reactivity on all POM clusters. For each cluster composition, ODH turnover rates reflect the reactivity-averaged HAE of all accessible O-atoms, which can be evaluated for each cluster composition to provide a rigorous and accurate predictor of ODH reactivity for catalysts with known structure. These relations together with oxidation reactivity measurements can then be used to estimate HAE values and to infer plausible structures for catalysts with uncertain active site structures.

1. INTRODUCTION

Keggin polyoxometalate (POM, $\text{H}_n\text{XM}_{12}\text{O}_{40}$) clusters are materials with known structures that remain uniform over a broad compositional range,^{1–5} thus allowing theoretical assessments of their thermodynamic and catalytic properties that are more accurate and reliable than those of supported oxide domains or bulk multicomponent oxides with less certain structures.^{6,7} These clusters consist of central tetrahedra (XO_4^{n-}) surrounded by metal oxide shells ($\text{M}_{12}\text{O}_{36}$) and charge-balancing protons (H_n^+); their redox and Brønsted acid properties place them among the most reactive solids reported for selective oxidation⁸ and acid-catalyzed⁹ reactions. As a result, these materials are well-suited for combining theory and experiment to assess reaction mechanisms and the effects of composition on reactivity and to establish rigorous relations

between catalyst properties and the dynamics and thermodynamics of elementary steps.

Oxidative dehydrogenation (ODH) reactions of alkanols and alkanes have been extensively studied using kinetic, isotopic, spectroscopic, and theoretical methods on many oxides.^{6,8,10–17} These reactions proceed via redox cycles^{12,18} with kinetic coupling between steps that reduce and reoxidize the catalysts; in most cases, H-atom transfer from the C–H bond in reactants to the lattice O-atoms in solids limits reaction rates. More specific details of the reaction mechanism, such as the nature of reactive species (molecular or dissociated)^{14,19} and active

Received: August 7, 2014

Revised: October 12, 2014

catalyst sites (bridging or terminal O-atoms of the oxide),^{20–22} as well as the nature of the relevant descriptors of O-atom reactivity, remain controversial.

CH₃OH ODH to HCHO has been typically proposed to proceed via methoxy species formed via quasi-equilibrated O–H dissociation before the rate-limiting C–H activation step.^{11,13–16} The involvement of dissociated methanol has been inferred by the detection of methoxy species from their vibrational spectra;¹⁴ some studies^{14,23} have shown, however, that such species are inert and act as spectator species that are often associated with support surfaces. Density functional theory (DFT) suggests that stable reactive methoxy species can form on isolated or small MO_x domains, either as gaseous clusters or embedded within tetrahedral SiO_x networks,^{24–28} but rate data show that such small domains are much less reactive than larger domains,^{6,7} suggesting that such model structures do not accurately represent the reactivity or mechanism of oxide domains in practical alkanol ODH reactions. Electron spin resonance spectra have led to proposals involving CH₂OH radical species formed via direct H-abstraction from molecular CH₃OH.¹⁹ Direct and rigorous comparisons between molecular and dissociative routes require the assessment of enthalpic and entropic factors that determine the relative contributions of these routes to turnover rates; this is possible, as we show here, only by combining experimental and theoretical studies carried out on well-defined and relevant oxide catalysts.

Here, we compare CH₃OH ODH turnover rates and kinetic and isotopic dependences measured on a Mo-based POM cluster (H₃PMo₁₂) with entropies and enthalpies of elementary steps derived from DFT and statistical mechanics treatments. In doing so, we assess the relevance of specific intermediate species and steps and compare the relevant kinetic parameters among POM clusters with different compositions (H₄SiMo₁₂, H₃PW₁₂, H₄PV₁Mo₁₁, and H₄PV₁W₁₁). This analysis leads to rigorous descriptors of reactivity in terms of H-atom addition energies (HAE), which measure the ability of O-atoms to activate C–H bonds through the late transition states that mediate the preferred molecular routes. Both enthalpy and entropy effects favor H-abstraction from molecular instead of dissociated methanol at all conditions relevant to the practice of ODH catalysis. The octahedral coordination of Mo addenda atoms, also prevalent in most oxide domains of catalytic relevance, hinders the insertion of the methanol O–H bond across Mo–O species and the formation of a Mo–OCH₃ bond; such steps are required for the formation of methoxy species. The transition state (TS) for H-abstraction from molecular CH₃OH is product-like and very late along the reaction coordinate; thus, its energy depends sensitively on the stability of the product O–H bond, which is assessed here by estimating HAE values at all accessible O-atoms. Calculated HAE values on bridging O-atoms are much more negative than those on terminal O-atoms for all catalysts, suggesting that H-abstraction occurs preferentially at bridging sites.

2. METHODS

2.1. Experimental Methods: Synthesis and Characterization of Supported Polyoxometalates and CH₃OH–O₂ Reaction Rate Measurements. SiO₂ (Cab-O-Sil, 304 m² g^{−1}, 1.5 cm³ g^{−1} pore volume) was washed with 1 M HNO₃ (10 cm³ (g-SiO₂)^{−1}) and treated in flowing dry air at 383 K overnight and at 573 K for 5 h before incipient wetness impregnation with solutions of H₃PMo₁₂O₄₀ (H₃PMo, 99.99%, Sigma-

Aldrich) in water (double-distilled and deionized; 1.5 cm³ solution per gram dry SiO₂) at ambient temperature. The POM concentration in water (0.102 g hydrated bulk POM per cm³ H₂O) was set to yield a theoretical surface density of 0.16 POM nm^{−2}, and the resulting sample is denoted henceforth as H₃PMo/SiO₂(0.16). The impregnated sample was stored in closed vials at ambient temperature for 24 h and then treated in flowing He (99.999%, Praxair) at 323 K for 24 h, pressed into wafers, crushed, and sieved to retain 106–180 μm aggregates.

Transmission electron microscopy, ³¹P Nuclear magnetic resonance spectroscopy measurements, and titrations with 2,6-di-*tert*-butylpyridine were used to probe the dispersion, Keggin structure of clusters, and accessibility to the acidic protons on supported clusters during reactions, respectively. The detailed procedures used in these measurements will be reported elsewhere; the resulting data showed that the supported clusters are well-dispersed intact Keggin, which can partially dehydroxylate and lose a fraction of their protons during thermal treatment or CH₃OH–O₂ reactions; kinetic and isotopic measurements described below were collected using a reference reaction condition that minimized such dehydroxylations by cofeeding H₂O (4 kPa H₂O, 20 kPa O₂, 2.7 kPa H₂O) and by returning to this condition after collecting each data point at a different pressure of reactants.

CH₃OH conversion rates and selectivities were measured at 403, 433, and 473 K using a tubular quartz reactor with plug-flow hydrodynamics. The temperature was set using a resistively heated furnace and a temperature controller (Watlow, Series 988) and measured with a K-type thermocouple (Omega) located within a dimple at the reactor wall. Samples were treated in 20 kPa O₂ (99.999%, Praxair, 0.5 cm³ s^{−1}) and 2.7 kPa H₂O by increasing the temperature at 0.05 K s^{−1} to the reaction temperature and holding for 0.5 h before exposing samples to reactants. Reactants consisted of mixtures of CH₃OH (99.9%, Fisher Scientific), O₂ (99.999%, Praxair), He (99.999%, Praxair), and H₂O (doubly distilled and deionized). He and O₂ were metered using mass flow controllers (Porter Instrument) while CH₃OH and H₂O were evaporated into flowing O₂/He streams at 393 K using separate liquid syringe pumps (Cole Parmer, 60061 Series) at molar rates adjusted to give the desired CH₃OH and O₂ pressures (0.15–4 and 20 kPa, respectively) and residence times (5–60 POM s CH₃OH^{−1}). CH₃OH conversions were below 20%, and all transfer lines after liquid injection were kept above 393 K to prevent condensation of reactants and products.

Reactant and product concentrations were measured by gas chromatography (Agilent 6890) using a methyl silicone capillary column (HP-1, 25 m × 0.32 mm × 1.05 μm) connected to a flame ionization detector and a Porapak Q packed column (80–100 mesh, 12 ft. × 1/8 in.) connected to a thermal conductivity detector. Dimethyl ether (DME), formaldehyde (HCHO), methyl formate (MF), dimethoxymethane (DMM), and H₂O were the only products detected. CH₃OH ODH rates (r_{ODH} ; normalized per POM cluster) are defined as the sum of HCHO, MF, and DMM molar formation rates ($r_{\text{ODH}} = r_{\text{HCHO}} + r_{\text{MF}} + r_{\text{DMM}}$) because these products all require the initial oxidation of one CH₃OH to HCHO (Supporting Information, Scheme S1).¹¹ Kinetic and thermodynamic constants were determined by simultaneously regressing measured rates to integral form of rate equations for ODH and DME formation, and their regressed values were used to extrapolate measured rates to zero residence times as described

in Supporting Information (section S.2); only the ODH rates are reported and analyzed in this work.

Kinetic isotope effects were measured using CH₃OH (99.9%, Fisher Scientific), CH₃OD (99.5%, Alfa Aesar), and CD₃OD (99.8%, Alfa Aesar) as reactants on H₃PtMo/SiO₂(0.16) to probe the kinetic relevance of steps involving C–H or O–H bond activation. The same experimental apparatus and protocols were used to perform reactions, measure effluent concentrations, and calculate rates with labeled and unlabeled methanol reactants.

2.2. Computational Methods. Periodic density functional theory calculations were performed using the Vienna ab initio Simulation Package (VASP).^{29,30} The Perdew–Wang implementation (PW91) of the generalized gradient approximation was used to describe electron exchange and correlation.³¹ A periodic plane wave basis-set expansion to a cutoff energy of 400 eV was used to represent valence electronic states; the interaction between valence and core electrons was described using the projector augmented wave (PAW) method.³² Electronic structures were converged self-consistently to energies $<1 \times 10^{-6}$ eV. Calculations were performed by specifying integer band occupancies with different spin multiplicities to determine the most stable electronic structure because reactive intermediates and transition states in ODH reactions may have partially filled d-orbitals with unpaired electrons and intermediates with diradical-type electronic structures.^{24,25} Singlet (no unpaired electrons) multiplicities were treated using both spin-restricted and spin-polarized calculations while doublet and triplet multiplicities were treated only as spin-polarized calculations. Some intermediates exhibited diradical structures,^{24,25} as indicated by greater stability of spin-polarized singlets than spin-restricted ones, which was further confirmed using broken-symmetry calculations using the Gaussian program,³³ with details as described below. Calculations were also performed using DFT+U methods, as implemented within VASP, to assess the effect of Hubbard model-based corrections to DFT energies on the calculated redox properties for systems with localized d-electrons.^{34–36}

Full Keggin clusters (~1.2 nm diameter) were calculated at the center of a $2 \times 2 \times 2$ nm³ unit cell to provide a vacuum region sufficient for preventing interactions among clusters in adjacent unit cells. A $1 \times 1 \times 1$ Monkhorst–Pack k-point mesh was used to sample the Brillouin zone. The structures of all stable intermediates were optimized until forces on atoms were <0.05 eV Å⁻¹. Dipole and quadrupole moments, calculated with the center of the unit cell taken as the center of charge, were used to correct for long-range interactions among neighboring unit cells. Transition states were located by using nudged elastic band (NEB) methods³⁷ to determine likely structures, which were then used to isolate transition states using Henkelman’s dimer method.³⁸ The electronic and geometric steps in NEB calculations were converged to energies $<1 \times 10^{-4}$ eV and to forces on atoms <0.2 eV Å⁻¹, respectively. The respective convergence criteria for dimer calculations were 1×10^{-7} eV and 0.05 eV Å⁻¹.

Vibrational frequencies required to estimate the thermodynamic properties of unlabeled and labeled reactive species and transition states were calculated by diagonalizing the Hessian matrix computed from two-sided finite differences of energy gradients and weighted by atomic masses for reactant molecules (CH₃OH, CD₃OD, and CH₃OD); the energy gradients were obtained by perturbing each atom in all three Cartesian

directions by ± 0.01 Å. These frequencies were used to derive vibrational partition functions.³⁹ Gibbs free energies were determined from statistical mechanics formalisms³⁹ involving translational and rotational and vibrational degrees of freedom for gaseous molecules and vibrational degrees of freedom for bare clusters and adsorbates. Low-frequency modes of weakly bound adsorbates lead to significant errors in estimation of vibrational partition functions and were either removed from partition functions or treated as translations or rotations similar to gaseous molecules (Supporting Information, section S.6). Kinetic isotope effects were calculated from the change in Gibbs free energies of H-abstraction transition states and reference states when H-atoms were replaced by D-atoms [KIE = $\exp(-(\Delta G_{TS}^H - \Delta G_{TS}^D)/RT)$].

Localized basis-set DFT calculations were performed using Gaussian³³ to compare the energies of ODH intermediates with those from periodic plane-wave calculations and to assess the effect of the exchange-correlation functional on the redox properties of POM cluster. PW91³¹ (DFT) and B3LYP^{40,41} (hybrid-DFT) functionals and double- ζ basis sets (Aug-cc-PVDZ-PP with core potentials for Mo and 6-31G(d,p) for H, C, O, and P atoms) were used. Energies and forces on atoms in these calculations were converged to $<1 \times 10^{-6}$ Ha and $<4.5 \times 10^{-3}$ Ha bohr⁻¹, respectively.

3. RESULTS AND DISCUSSION

3.1. ODH Turnover Rates with CH₃OH-O₂, CD₃OD-O₂, and CH₃OD-O₂ Mixtures. CH₃OH dehydration reactions to form dimethyl ether (DME) (on H⁺) and ODH reactions to form formaldehyde (HCHO) (on O-atoms) occur concurrently on POM cluster (Supporting Information, Scheme S.1). Figure 1 shows CH₃OH ODH rates (r_{ODH}) per POM cluster

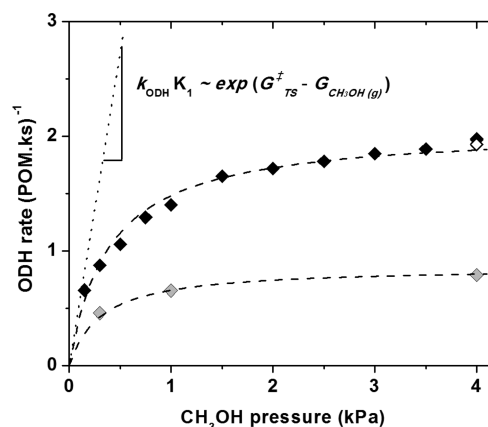


Figure 1. Measured ODH rates per POM cluster for CH₃OH (black symbols), CH₃OD (white symbols), and CD₃OD (gray symbols) reactants as a function of methanol pressure on H₃PtMo/SiO₂(0.16) (433 K, 20 kPa O₂). Reported rates were extrapolated to zero conversion using the integral form of rate equations. Dashed curves represent regressed best-fits of the extrapolated rates to the form of eq 4. Dotted line reflects initial slope of ODH rates with respect to CH₃OH pressure.

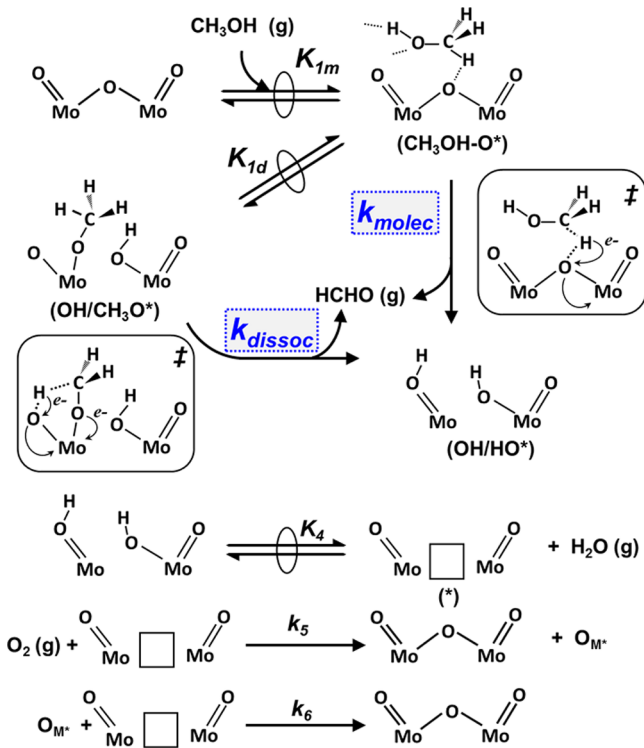
on H₃PtMo/SiO₂(0.16) as a function of CH₃OH pressure (0.15–4.0 kPa) at 20 kPa O₂. At low CH₃OH pressures, ODH rates increased linearly with pressure, but then more gradually at higher pressures, indicative of a Langmuir-type rate equation:

$$\frac{r_{\text{ODH}}}{[\text{POM}]} = \frac{\alpha P_{\text{CH}_3\text{OH}}}{1 + \beta P_{\text{CH}_3\text{OH}}} \quad (1)$$

This dependence of r_{ODH} on CH_3OH pressure ($P_{\text{CH}_3\text{OH}}$) is consistent with Mars–van Krevelen redox cycles,^{12,18} involving the kinetic coupling of reduction and reoxidation of active centers, with the reduction part of the cycle as the sole kinetically-relevant step. Many of the previous studies on CH_3OH and $\text{CH}_3\text{CH}_2\text{OH}$ ODH on supported MoO_x ,^{10,13,14} iron-molybdate,¹² VO_x ,¹⁵ and RuO_x ¹⁶ catalysts have assumed, often implicitly and without independent evidence, that in the reduction step, alkanols first dissociate and then undergo H-abstraction from adsorbed alkoxy species. The rate equations developed from these assumptions, however, are identical to those that would be developed if H-abstraction occurred instead from molecularly adsorbed alkanols. Both of these routes have sequences of elementary steps that are consistent with the functional form of eq 1, but each assigns a different chemical significance to the α and β parameters. DFT-derived energetics for these routes, shown in section 3.2, provide compelling evidence for the prevalence of C–H activation from adsorbed molecular CH_3OH instead of methoxy species.

Scheme 1 shows the respective sequences of elementary steps for dissociative and molecular methanol ODH routes; they diverge after the initial quasi-equilibrated adsorption of gaseous CH_3OH at lattice O-atoms (O^*) as intact molecular

Scheme 1. Proposed Elementary Steps for CH_3OH ODH on MoO_x via Molecular and Dissociative Routes^a



^aMolecular and dissociative routes involve H-abstraction from molecularly adsorbed CH_3OH and dissociated methoxy species, respectively, in the kinetically-relevant step, leading to HCHO and the reduced oxide catalyst. The reduction of oxide is followed by fast reoxidation steps that may involve recombination of OH-pairs and O-vacancies that react with O_2 .

species ($\text{CH}_3\text{OH-O}^*$, Scheme 1). In the dissociative route, these $\text{CH}_3\text{OH-O}^*$ species dissociate to form vicinal surface hydroxide–methoxy pairs ($\text{OH/CH}_3\text{O}^*$, shown as a quasi-equilibrated step in Scheme 1) and then undergo irreversible H-abstraction from CH_3O^* by a lattice O-atom. This H-abstraction step releases HCHO into the gas phase, in a step that causes metal centers to undergo a two-electron reduction and forms two vicinal OH species (OH/HO^*), which ultimately form H_2O as the other product of ODH events. The molecular route involves the sequential abstraction of H atoms from the C and O atoms in molecular ($\text{CH}_3\text{OH-O}^*$) species, using vicinal O^* species to form HCHO and OH pairs (OH/HO^*). The first H-abstraction is the kinetically-relevant step for this route, and each of the two steps causes a one-electron reduction of the POM cluster. In both routes, the (OH/HO^*) species undergo quasi-equilibrated recombination–dissociation steps to form gaseous H_2O and an O-vacancy (O^*). A turnover is completed by irreversible O_2 dissociation (step 5 in Scheme 1), which reoxidizes the second O-vacancy by migration of one of the O-atoms in O_2 (O_M^*) (step 6 in Scheme 1); the mechanistic details of these reoxidation steps are uncertain and the subject of current study, but they are, in the context of this study and of practical ODH catalysis, fast and thus kinetically-irrelevant.²⁵

A pseudo-steady-state treatment of surface intermediates and the assumptions of quasi-equilibrated molecular adsorption of CH_3OH and its dissociation to form methoxy species, quasi-equilibrated recombination of OH pairs (or dissociation of H_2O at O^*), irreversible H-abstractions (from methoxy and from C and O atoms of CH_3OH), and irreversible reoxidation of O-vacancies lead to a rate equation of the form (derivation in Supporting Information, section S.2)

$$\frac{r_{\text{ODH}}}{[\text{POM}]} = \frac{(k_{\text{molec}}K_{1\text{m}} + k_{\text{dissoc}}K_{1\text{m}}K_{1\text{d}})P_{\text{CH}_3\text{OH}}}{1 + K_{1\text{m}}(1 + K_{1\text{d}})P_{\text{CH}_3\text{OH}} + \frac{(k_{\text{molec}}K_{1\text{m}} + k_{\text{dissoc}}K_{1\text{m}}K_{1\text{d}})P_{\text{CH}_3\text{OH}}}{2k_5P_{\text{O}_2}} \left(1 + \frac{P_{\text{H}_2\text{O}}}{K_4}\right)} \quad (2)$$

$\begin{array}{c} | \quad | \quad | \\ \text{[O}^*] \quad \text{[CH}_3\text{OH-O}^*] \quad \text{[OH/CH}_3\text{O}^*] \\ | \quad | \\ \text{[*]} \quad \text{[OH/HO}^*] \end{array}$

The rate and equilibrium parameters in this equation are defined in Scheme 1. The denominator terms in eq 2 reflect coverages of different surface species relative to O^* . At the high O_2 -to- CH_3OH ratios ($\text{O}_2/\text{CH}_3\text{OH} > 1$) used in this study, measured ODH rates were independent of O_2 pressure, suggesting that the coverage of reduced centers is much smaller than that of O^* ($[\text{*}] + [\text{OH/HO}^*] \ll 1$). Therefore, the rate equation can be simplified to the following form for molecular route:

$$\frac{r_{\text{ODH,molec}}}{[\text{POM}]} = \frac{k_{\text{molec}}K_{1\text{m}}P_{\text{CH}_3\text{OH}}}{1 + K_{1\text{m}}(1 + K_{1\text{d}})P_{\text{CH}_3\text{OH}}} \quad (3)$$

and for its dissociative counterpart

$$\frac{r_{\text{ODH,dissoc}}}{[\text{POM}]} = \frac{k_{\text{dissoc}}K_{1\text{m}}K_{1\text{d}}P_{\text{CH}_3\text{OH}}}{1 + K_{1\text{m}}(1 + K_{1\text{d}})P_{\text{CH}_3\text{OH}}} \quad (3')$$

Equations 3 and 3' both have a functional form that suggests a change in the most abundant surface intermediate from unoccupied O^* to molecular or dissociated adsorbed species as CH_3OH pressure increases and that each can contribute to total ODH rates. When only one of these two routes prevails, the total ODH rates can be described by

$$\frac{r_{\text{ODH}}}{[\text{POM}]} = \frac{k_{\text{ODH}}K_1P_{\text{CH}_3\text{OH}}}{1 + K_1P_{\text{CH}_3\text{OH}}} \quad (4)$$

where k_{ODH} and K_1 reflect the constants k_{molec} and $K_{1\text{m}}$ (defined in Scheme 1), respectively, for the molecular route and k_{dissoc} and $K_{1\text{m}}K_{1\text{d}}$ (Scheme 1), respectively, for the dissociative route.

The slope of the rate data in Figure 1 at low CH_3OH pressures ($1 \gg K_1P_{\text{CH}_3\text{OH}}$) gives the value of the first-order rate constant $k_{\text{ODH}}K_1$ in eq 4. This rate constant reflects the free energy of the H-abstraction TS (G_{TS}^\ddagger) relative to an uncovered surface (G_{O^*}) and a gaseous CH_3OH molecule ($G_{\text{CH}_3\text{OH}(\text{g})}$)

$$k_{\text{ODH}}K_1 \sim \exp(- (G_{\text{TS}}^\ddagger - G_{\text{O}^*} - G_{\text{CH}_3\text{OH}(\text{g})})/RT) \quad (5)$$

Turnover rates become independent of CH_3OH at high pressures ($1 \ll K_1P_{\text{CH}_3\text{OH}}$, eq 4) and are given by zero-order rate constant k_{ODH} , which reflects the free energy of the same TS but relative to an adsorbed CH_3OH (instead of gaseous) molecule ($G_{\text{CH}_3\text{OH}(\text{a})}$):

$$k_{\text{ODH}} \sim \exp(- (G_{\text{TS}}^\ddagger - G_{\text{CH}_3\text{OH}(\text{a})})/RT) \quad (6)$$

When the molecular route prevails, G_{TS}^\ddagger and $G_{\text{CH}_3\text{OH}(\text{a})}$ values in eqs 5 and 6 reflect free energies of the molecular H-abstraction TS and the molecularly adsorbed $\text{CH}_3\text{OH-O}^*$, respectively. When the dissociative route prevails, G_{TS}^\ddagger and $G_{\text{CH}_3\text{OH}(\text{a})}$ values reflect free energies of the dissociative H-abstraction TS and the dissociated methanol present as methoxy species ($\text{OH/CH}_3\text{O}^*$), respectively.

Scheme 1 includes the kinetically-relevant H-abstraction step at the C–H (instead of the O–H) bond in CH_3OH , an assumption that cannot be validated from the CH_3OH rate data in Figure 1 alone; the relative rates of molecules labeled with D-atoms at the C or O in CH_3OH , however, can discern which vibrational modes are involved in the reaction coordinate leading to the kinetically-relevant transition state.⁴² ODH rates for CH_3OD and CH_3OH reactants were similar, but those for CD_3OD were much lower (Figure 1). Kinetic isotope effects (KIE), defined as the ratio of rate constants regressed from rate data to the form of eq 4 (e.g., first-order KIE = $k_{\text{ODH}}K_{1,\text{CH}_3\text{OH}}/k_{\text{ODH}}K_{1,\text{CD}_3\text{OD}}$ or $k_{\text{ODH}}K_{1,\text{CH}_3\text{OH}}/k_{\text{ODH}}K_{1,\text{CH}_3\text{OD}}$) are shown in Table 1. KIE values for CH_3OD were near unity, but those for CD_3OD were much larger (1.9 ± 0.5 and 2.4 ± 0.3 for first- and zero-order rate constants, respectively; Table 1). A large KIE value for C–D and a value near unity for O–D are consistent with previous reports for methanol and ethanol on VO_x domains^{15,16} and with the kinetic relevance of H-abstraction from the C-atom (instead of the O-atom) in methanol. These KIE values, however, cannot discern whether C–H activation occurs from molecular or dissociated forms of adsorbed methanol ($\text{CH}_3\text{OH-O}^*$ vs $\text{OH/OCH}_3\text{-O}^*$) because thermodynamic isotope effects for both species are likely to be near unity. While many previous studies have implicitly assumed that H-abstraction occurs from methoxy species,¹⁴ rate equation and isotopic effects can neither confirm nor invalidate such assumptions; their assessment must rely instead on rigorous theoretical methods using catalytic structures that are well-defined and thus amenable to such treatments.

The rates of chemical reactions depend on free-energy differences between transition states and their relevant precursors. The functional form of Gibbs free energies favors enthalpic over entropic stabilization of transition states⁴³ at

Table 1. Ratios of First-Order ($k_{\text{ODH}}K_1$) and Zero-Order (k_{ODH}) Rate Constants for Unlabeled (CH_3OH) and Labeled (CD_3OD or CH_3OD) Reactants Derived from Periodic DFT (PW91-PAW) Calculations for Molecular and Dissociative Routes and the Corresponding Values Measured Experimentally on $\text{H}_3\text{PMo}_{12}\text{O}_{40}$ Clusters at 433 K

reaction route	structures	$(\text{CH}_3\text{OH}/\text{CD}_3\text{OD})$		$(\text{CH}_3\text{OH}/\text{CH}_3\text{OD})$	
		$k_{\text{ODH}}K_1$	k_{ODH}	$k_{\text{ODH}}K_1$	k_{ODH}
dissociative (Figure 3b) ^a	D1-TSb3	2.2	3.2	0.9	1.0
	D1-TSt1	2.0	3.0	0.9	1.0
molecular (Figure 3b) ^a	M2-TSb3	2.3	2.7	0.9	0.9
	M1-TSb3	2.4	2.9	0.9	1.0
experiment ^b		1.9 (± 0.5)	2.4 (± 0.3)	–	1.0

^aCalculated from ΔG values. Isotopic effects for translations and rotations in the gas-phase and respective low-frequency vibrations in adsorbed species were removed. ^bMeasured on $\text{H}_3\text{PMo}/\text{SiO}_2(0.16)$ at 20 kPa O_2 . Uncertainties reflect 95% trust intervals.

modest temperatures, while entropic effects typically prevail at high temperatures. Transition-state theory formalisms give the ratio of ODH turnover rates via the molecular and the dissociative route (eq 3 and 3') as

$$\frac{r_{\text{ODH,molec}}}{r_{\text{ODH,dissoc}}} = \exp\left(\frac{-(\Delta G_{\text{molec}}^\ddagger - \Delta G_{\text{dissoc}}^\ddagger)}{RT}\right) = \chi \quad (7)$$

where $\Delta G_{\text{molec}}^\ddagger$ and $\Delta G_{\text{dissoc}}^\ddagger$ represent free-energy differences between the transition states involved in molecular and dissociative routes and the same gaseous CH_3OH and uncovered redox sites in POM clusters, respectively. The value of χ accounts for the relative contributions of molecular and dissociative routes at each temperature and is independent of CH_3OH pressure. The free energies in eq 7 can be related to enthalpy and entropy differences between the two transition states

$$\Delta G_{\text{molec}}^\ddagger - \Delta G_{\text{dissoc}}^\ddagger = (H_{\text{molec}}^\ddagger - H_{\text{dissoc}}^\ddagger) - T(S_{\text{molec}}^\ddagger - S_{\text{dissoc}}^\ddagger) \quad (8)$$

which can be estimated by theoretical treatments based on DFT and statistical mechanics, as we show in the next section.

3.2. Theoretical Treatments of Molecular and Dissociative ODH Routes. ODH reaction pathways were determined using periodic DFT calculations to explore all anticipated structures and conformations of molecular and dissociative CH_3OH adsorption near the bridging (O_{b3} , O_{b7}) and terminal (O_{t1}) O-atoms surrounding a particular Mo-atom (Mo_1) of $\text{H}_3\text{PMo}_{12}\text{O}_{40}$ cluster with a nearby acidic proton (H^+) (atom locations shown in Supporting Information, Figure S.1) and calculating C–H activation TS energies (ΔE) from these adsorbed intermediates. Figure 2 compares the molecular and dissociative routes with the smallest ΔE values of activation (among the calculated structures) for each route; the molecular route involves H-bonding interactions with an H^+ -atom and H-abstraction by the O_{b3} atom, while the dissociative route involves H-abstraction from $\text{Mo}_1\text{-OCH}_3$ by the O_{t1} atom. Other calculated structures involving different adsorbate geometries and O-atoms used for H-abstraction are shown in Figure 3.

The entry step involves molecular adsorption of CH_3OH on $\text{H}_3\text{PMo}_{12}\text{O}_{40}$ clusters, irrespective of whether C–H bonds are

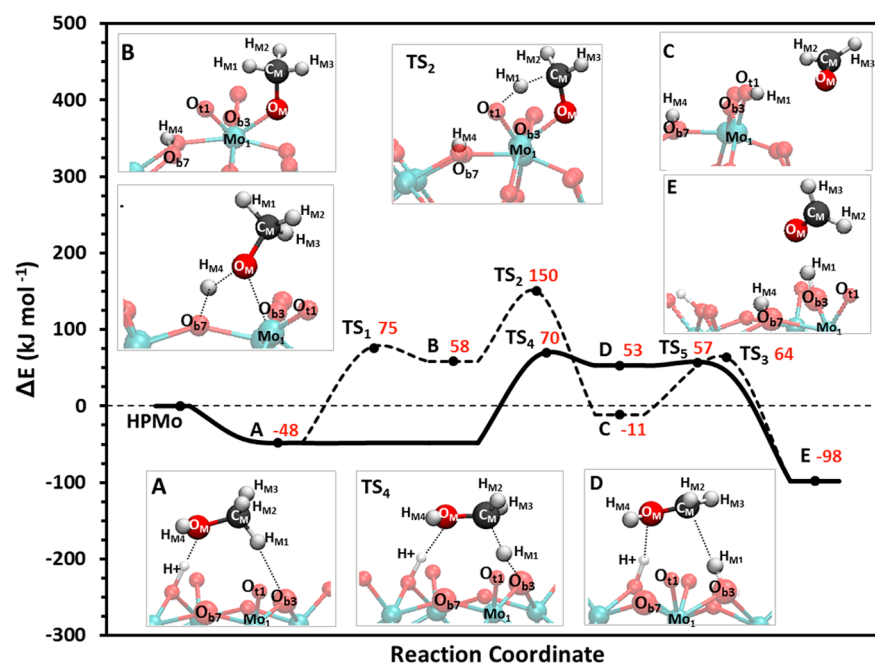


Figure 2. Structures and energies (ΔE) of intermediates and transition states calculated for CH_3OH ODH reaction involving dissociative (dashed curve) and molecular routes (solid curve) on $\text{H}_3\text{PMo}_{12}\text{O}_{40}$ clusters. Labels on atoms correspond to those used to report bond distances in the text and in Figure 3.

eventually activated before or after O–H dissociation. CH_3OH can adsorb near an acidic proton via strong H-bonding between the H^+ and the O_M -atom in CH_3OH (Figure 2, structure A) or far from H^+ species via weaker H-bonding between the H-atoms (H_{M1} and H_{M4}) in CH_3OH and the O-atoms (O_{b3} and O_{b7}) in the POM clusters; in both cases, adsorption–desorption events have low activation barriers in both directions, leading to their quasi-equilibrium with gaseous CH_3OH . Adsorption near an H^+ is more exothermic than in the case of interactions solely with O-atoms in POM clusters (Figure 3a, $\Delta E = -48$ and -7 kJ mol^{-1} for M2 and M1, respectively); their reaction energies (ΔE) reflect DFT-derived energies corresponding to those for the equilibrium constant for molecular adsorption (K_{1m} , Scheme 1).

The O_M – H_{M4} bond in adsorbed CH_3OH can dissociate (via TS_1 , Figure 2) to form a vicinal hydroxide (O_{b7} – H_{M4}) and a methoxy (Mo_1 – O_MCH_3) (structure B in Figure 2). This step is endothermic on POM clusters ($\Delta E = +58$ kJ mol^{-1} , structure B) because the octahedral coordination of Mo-atoms imposes significant steric constraints in accessing Mo-centers, which is required to form the Mo – OCH_3 bond; previous DFT treatments suggest that such access may well be more facile in VO_x and MoO_x monomers embedded in a tetrahedral SiO_x network,^{24,25} but such materials are much less reactive than extended oxide domains that form octahedral structures,^{6,7} making the conclusions largely confined to what appear to be minority routes in relevant catalytic solids.^{6,7} The endothermic nature of methoxy formation on octahedral Mo oxide structures and the significant entropy penalties in forming such sterically hindered Mo – OCH_3 species suggest that they represent minority species at working catalytic surfaces ($K_{1d} \ll 1$ in Scheme 1).

Methoxy species, if formed, can undergo H-abstraction by a terminal O-atom (O_{t1} used here as an example) in the POM cluster via a transition state (TS_2 , Figure 2) that requires the concerted transfer of two electrons into Mo d-orbitals in a

single step that forms gaseous HCHO and vicinal OH-pairs (structure C, Figure 2). The abstracted H-atom then transfers from a terminal O_{t1} -atom to a more stable bridging O_{b3} -atom via a proton-hopping step (TS_3 and structure E, Figure 2), which occurs after the kinetically-relevant H-abstraction; therefore, the activation barrier for TS_2 does not benefit from the greater stability of the O_{b3} – H_{M1} bond relative to that of the O_{t1} – H_{M1} bond. The energy barrier for H-abstraction from methoxy species (92 kJ mol^{-1} ; TS_2 , Figure 2) is much higher than the barrier for reverting to molecularly adsorbed CH_3OH (17 kJ mol^{-1} ; TS_1 , Figure 2), suggesting that O–H dissociation would be quasi-equilibrated, but C–H bond activation in methoxy species is a difficult and kinetically-relevant step in such dissociative routes. These DFT-derived energies are thus consistent with the proposed elementary steps in Scheme 1 and the proposed rate equation (eq 3'). The TS energy for the H-abstraction step relative to gaseous methanol corresponds to the first-order rate constant (eq 5, $k_{\text{ODH}}K_1 = k_{\text{dissoc}}K_{1m}K_{1d}$; $\Delta E_{k_{\text{ODH}}K_1}^\ddagger = 150$ kJ mol^{-1} , Figure 2), while the difference between energies of the TS and the methoxy species reflects the zero-order rate constant (eq 6, $k_{\text{ODH}} = k_{\text{dissoc}}$; $\Delta E_{k_{\text{ODH}}}^\ddagger = 92$ kJ mol^{-1} , Figure 2). The high activation energy for this C–H activation step (150 kJ mol^{-1}) and the endothermic nature of methoxy formation (58 kJ mol^{-1}), however, make this route improbable as the mechanism for ODH turnovers.

The alternate route involves a direct reaction of molecularly adsorbed CH_3OH with O-atoms (O_{b3} used as an example, Figure 2) in POM clusters. In this route, the H-abstraction occurs sequentially, first from the C–H bond and then from the O–H bond of CH_3OH ; attempts to calculate concerted C–H and O–H activations invariably led to sequential pathways in converged calculations (energy profiles for NEB calculations³⁷ shown in Supporting Information, Figure S.2). The C–H activation step involves the transfer of a single electron into the POM cluster (TS_4 , Figure 2) from adsorbed CH_3OH molecule

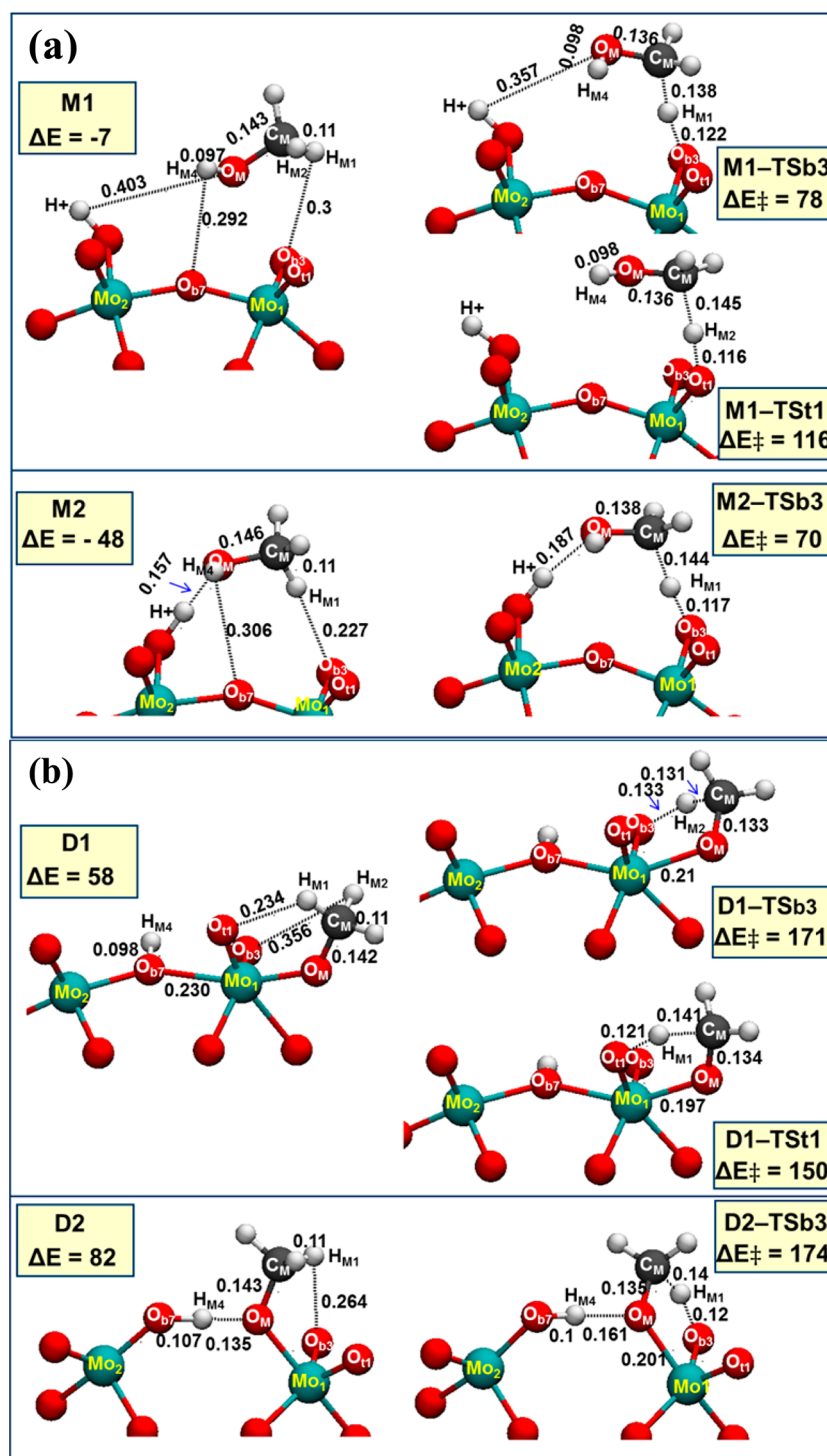


Figure 3. Structures, energies (kilojoules per mole) and bond distances (nanometers) for different structures of adsorbed species (methoxy or CH_3OH) and transition states for CH_3OH ODH on $H_3PMo_{12}O_{40}$ cluster via (a) molecular (M1, M2) and (b) dissociative (D1, D2) routes. M1 involves CH_3OH adsorption away from acidic H^+ -atom via weak H-bonding while M2 involves adsorption close to H^+ via strong H-bonding. D1 involves methoxy formation without significantly altering lattice Mo–O connectivity, while D2 involves insertion of O_M-H_{M4} from CH_3OH between the lattice Mo_1-O_{b7} bond. TSb3 and TSt3 are transition states for H-abstraction via bridging (O_{b3}) and terminal (O_{t1}) O-atoms, respectively.

with a barrier ($\Delta E^\ddagger = 70 \text{ kJ mol}^{-1}$) that is much smaller than for the similar H-abstraction from methoxy species ($\Delta E^\ddagger = 150 \text{ kJ mol}^{-1}$) and does not require the endothermic coordination of OCH_3 groups to Mo centers. The result of this C–H activation step is the formation of radical-like CH_2OH species (structure D, Figure 8; $\Delta E = +53 \text{ kJ mol}^{-1}$) analogous to those derived

from DFT treatments of C–H activation in alkanes on VO_x domains, which also have a diradical intermediate in which an alkyl radical interacts with a H–O–V site.^{44–46} In CH_3OH reactions, a vicinal lattice O-atom (O_{b7} in this example) then abstracts the second H-atom from the O–H bond in unstable CH_2OH radicals in a subsequent and kinetically-irrelevant step

($\Delta E^\ddagger = +57 \text{ kJ mol}^{-1}$ TS_S, Figure 2) that is essentially barrierless and appears as an energy “ledge” along the reaction coordinate that forms HCHO from CH₃OH (TS_S, Figure 2; NEB³⁷ energy profiles in Supporting Information, Figure S.2). The TS energy for the C–H activation step relative to gaseous methanol corresponds to the temperature-dependent part of the first-order rate constant (eq 5, $k_{\text{ODH}}K_1 = k_{\text{molec}}K_{1m}$; $\Delta E_{k_{\text{ODH}}K_1}^\ddagger = 70 \text{ kJ mol}^{-1}$, Figure 2), while the difference between energies of the TS and the H-bonded CH₃OH species reflects the temperature-dependent part of the zero-order rate constant (eq 6, $k_{\text{ODH}} = k_{\text{molec}}$; $\Delta E_{k_{\text{ODH}}}^\ddagger = 118 \text{ kJ mol}^{-1}$, Figure 2). The O-atom of CH₃OH in the molecular route TS is not attached to Mo centers, suggesting that the TS can benefit from the significant entropy gains made possible by rotational freedom in adsorbed species. These DFT-derived energy barriers, and the anticipated entropic differences, indicate that H-abstraction from molecular CH₃OH is overwhelmingly preferred, as it is a more facile route for oxidative methanol activation because it avoids steric effects associated with access to Mo centers and the high barriers associated with C–H activation in methoxy species; the latter involves a simultaneous two-electron reduction of POM clusters instead of the sequential two one-electron reduction events involved in the activation of C–H and O–H bonds in molecular routes. Two one-electron reductions are favored over a two-electron reduction in the kinetically-relevant step, as indicated by more negative reduction potentials required for the second electron.⁴⁷

Figure 3 shows alternate structures and the respective energies of kinetically-relevant transition states and their adsorbed precursor species involved in these molecular and dissociative routes. Molecular CH₃OH adsorption can occur via weak H-bonding (Figure 3a, structure M1; H⁺–O1 distance, 0.403 nm; $\Delta E = -7 \text{ kJ mol}^{-1}$) or a strong H-bonding (Figure 3a, structure M2; H⁺–O1 distance, 0.157 nm; $\Delta E = -48 \text{ kJ mol}^{-1}$), with concomitantly lower entropies for the latter because of restricted surface mobility. The weak or strong adsorption of this species determines the value of adsorption equilibrium constant (denominator term in eq 3) and the reference state for zero-order rate constant (eq 6) while the first-order rate constant depends only on the free energy of the TS relative to that for the gaseous reactant (eq 5). The strongly H-bonded species are unlikely to prevail during steady-state catalysis because protons are predominantly titrated with H-bonded monomers or protonated dimers, which act as intermediates in methanol dehydration to DME (Supporting Information, Scheme S.1). Such strong H-bonded species would also have to access O* sites reactive for ODH, which would involve proton mobility without the concerted stabilization provided by O-atoms. The weakly bound CH₃OH retains significant translation at surfaces and can access all O* sites (as discussed below, section 3.3); it can transfer a H-atom to bridging or terminal O-atoms, but the TS is much more stable when bridging O-atoms are involved (Figure 3a, M1-TSb3; $\Delta E^\ddagger = +78 \text{ kJ mol}^{-1}$; M1-TSt1; $\Delta E^\ddagger = +116 \text{ kJ mol}^{-1}$), consistent with H–O_{b3} bonds stronger than H–O_{t1} bonds in the products of this elementary step (section 3.5). A strongly H-bonded CH₃OH molecule must lose its stabilization by the H⁺ at the TS; therefore, its TS for H-abstraction is only slightly more stable (Figure 3a, M2-TSb3; $\Delta E^\ddagger = +70 \text{ kJ mol}^{-1}$) than their weakly H-bonded counterparts at each distinct O-atom in the POM cluster.

Methoxy species involved in dissociative routes can assume several configurations, as shown by DFT calculations (Figure 3b; Supporting Information, section S.5). One of these configurations avoids significant disruption of Mo–O connectivity before inserting a new Mo–OCH₃ bond (Figure 3b, structure D1, $\Delta E = +58 \text{ kJ mol}^{-1}$), while another one requires cleavage of Mo₁–O_{b7} bonds and insertion of H_{M4}–O_M bonds of methanol molecule within the lattice (Figure 3b, structure D2; $\Delta E = +82 \text{ kJ mol}^{-1}$). This latter structure has been proposed to be involved in CH₃OH dissociation on isolated VO_x monomers²⁴ and benefits from H-bonding interactions between H_{M4} and O_M; however, this configuration is much less stable than the D1 structure on POM clusters, evidently because of steric effects. H-abstraction TS energies are very similar for these two methoxy configurations at each distinct O-atom in POM clusters (Figure 3b; $\Delta E^\ddagger = +171$ and $+174 \text{ kJ mol}^{-1}$ for D1-TSb3 and D2-TSb3, respectively). In contrast with the molecular route, H-abstraction from methoxy species occurs more readily via reactions with terminal (Figure 3b, D1-TSt1; $\Delta E^\ddagger = +150 \text{ kJ mol}^{-1}$) instead of bridging (Figure 3b, D1-TSb3; $\Delta E^\ddagger = +171 \text{ kJ mol}^{-1}$) O-atoms because the basicity of the terminal O-atoms increases and allows stronger O–H bonds when a methoxy group is attached to a Mo-atom (section 3.5, Table 3).

Other CH₃OH adsorption geometries involving migration of methoxy (O_MCH₃) species to bridging (O_{b3}) or terminal (O_{t1}) O-atoms or of H_{M4} atom to a distant O_{b1} atom, dissociation of methanol using terminal O_{t1} atom, and H-abstraction from Mo–OCH₃ using a O* or the OH* species formed during dissociation step were also explored (Supporting Information, section S.5). The energies of all these geometries were either significantly higher or nearly identical to those reported in Figures 2 and 3 (Supporting Information, section S.5). In all cases and for all possible structures, DFT-derived energies show that molecular routes are much more facile than dissociative routes.

3.3. Kinetic Isotope Effects and Enthalpy and Entropy Changes for Rate Constants in Molecular and Dissociative Routes. First- and zero-order ODH rate constants reflect the free energies of H-abstraction TS structures referenced to gaseous CH₃OH (eq 5) and molecular or dissociative adsorbed methanol species (eq 6), respectively. KIE values for these rate constants reflect the respective changes in these free-energy differences between the transition states and their reference states when unlabeled reactants are replaced by labeled reactants. Replacement of C–H bonds by C–D decreases the corresponding stretching vibrational energy in the reference states, but not in the C–H activation TS, because the stretching vibrational mode lies along the reaction coordinate, which leads to higher free energies of activation (for C–D than for C–H) and KIE values greater than unity. DFT-derived KIE values for first- and zero-order ODH rate constants for two different TS structures in molecular (Figure 3a; M1-TSb3, weak H-bonded; and M2-TSb3, strong H-bonded) and dissociative (Figure 3b; D1-TSb3, H-abstraction by terminal O; and D1-TSt1, H-abstraction by bridging O) routes and measured KIE values are shown in Table 1. The transition states for both routes gave KIE values close to unity with CH₃OD reactants and values well above unity for CD₃OD reactants for first-order (2.2 to 2.4, Table 1) and zero-order (2.7 to 3.2, Table 1) rate constants, consistent with measured values (1.9 ± 0.5 and 2.4 ± 0.3 , respectively, Table 1) and with kinetically-relevant TS structures involving the cleavage of a C–

H bond (but not an O–H bond). Thus, KIE values cannot discern between molecular and dissociative routes, but the much higher barriers for the latter routes clearly show that methanol ODH occurs solely via kinetically-relevant H-abstraction from molecularly adsorbed methanol.

Figure 4 shows measured first-order rate constants ($k_{\text{ODH}}K_1$) and CH_3OH adsorption equilibrium constants (K_1) as a

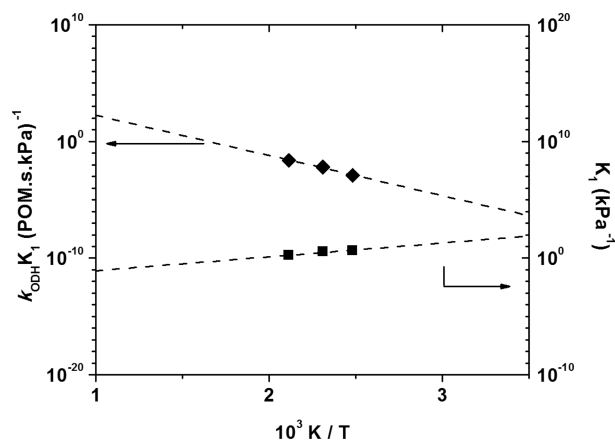


Figure 4. Measured first-order ODH rate constants ($k_{\text{ODH}}K_1$) and CH_3OH adsorption equilibrium constants (K_1) as a function of reciprocal temperature on $\text{H}_3\text{PMo}/\text{SiO}_2(0.16)$ at 403, 433, and 473 K (20 kPa O_2).

function of reciprocal temperature. The slopes and intercepts in these plots are used to estimate the experimental enthalpy and entropy values, respectively, for each of these parameters. Table 2 compares these measured enthalpies and entropies with values derived from statistical mechanics formalisms for two possible sets of intermediates and transition states corresponding to each of the two routes: dissociative (D1-TSt1 and D1-Tsb3, Figure 3b; H-abstraction by terminal or bridging O) and molecular (M1-TSb3 and M2-Tsb3, Figure 3b; weak or strong H-bonded CH_3OH). Two types of species are considered as intermediates for each route because they differ only slightly in

their stability, as inferred from their DFT-derived formation energies, and any differences in their entropy may determine their prevalence. Measured enthalpies of formation of ODH transition states from gaseous CH_3OH ($\Delta H_{k_{\text{ODH}}K_1}^\ddagger = 62 \pm 15 \text{ kJ mol}^{-1}$) resemble DFT-derived values for both strong and weak H-bonded molecular routes (53 and 61 kJ mol^{-1} , respectively; Table 2), but not those for dissociative routes (158 and 138 kJ mol^{-1} ; Table 2). Closer agreement is not expected between theory and experiment because (i) DFT values reflect the properties of only one of the 24 bridging and 12 terminal O^* -atoms (O_{b3} , Supporting Information, Figure S.1) in a POM cluster, while CH_3OH molecules sample all O-atoms according to their reactivities during catalytic experiments; (ii) interactions of protons with CH_3OH , as part of concurrent dehydration reactions (Supporting Information, Scheme S.1), can slightly influence the H-abstrating properties of all O-atoms in POM clusters; and (iii) DFT-derived energies vary slightly with the specifics of the theoretical treatments such as the functionals (e.g., DFT or hybrid DFT) and basis sets (periodic plane-waves or molecular) used. Nevertheless, molecular routes agree with measured enthalpies within the bounds of such inaccuracies, while dissociative routes lie well outside such bounds by all accepted estimates of uncertainties.

The entropies of transition states and relevant intermediates were estimated from DFT-derived frequencies obtained using the harmonic approximation, which provides inaccurate estimates of entropy contributions from the low-frequency vibrational modes characteristic of loosely bound species.⁴⁸ Therefore, such modes (frequencies $<110 \text{ cm}^{-1}$) were treated explicitly as translational and rotational modes similar to gaseous CH_3OH .³⁹ The calculated frequencies and their contribution to enthalpies and entropies for each intermediate and TS structure in Table 2 are shown in the Supporting Information (Tables S.6–S.11). Molecular CH_3OH adsorbed via weak H-bonds (Figure 3a, M1) exhibited the largest number (five) of low-frequency modes that resemble the translational and rotational modes of gaseous CH_3OH . These frequencies were removed from vibrational partition functions, and their enthalpic and entropic contributions were treated as those

Table 2. Periodic DFT (PW91-PAW) Derived Changes in Electronic Energies (ΔE), Zero-Point Energy Corrected Energies [$\Delta(E+\text{ZPE})$], Enthalpies (ΔH), Entropies (ΔS), and Free Energies (ΔG) Corresponding to the First-Order Rate Constant ($k_{\text{ODH}}K_1$) and CH_3OH Adsorption Equilibrium Constant (K_1) for Molecular and Dissociative Routes (Calculated Structures of Relevant Species Shown in Figure 3), and the Respective ΔH , ΔS , and ΔG Values Measured on $\text{H}_3\text{PMo}/\text{SiO}_2(0.16)$ (Figure 4)

	dissociative (Figure 3b)		molecular (Figure 3a)		measured ^c
	D1-TSb3	D1-TSt1	M2-TSb3	M1-TSb3	
$\Delta E_{k_{\text{ODH}}K_1}^\ddagger$ ^a	171	150	70	78	–
$\Delta(E+\text{ZPE})_{k_{\text{ODH}}K_1}^\ddagger$ ^a	160	141	56	64	–
$\Delta H_{k_{\text{ODH}}K_1}^\ddagger$ ^b	153 (156)	132 (136)	48 (53)	56 (61)	62 (± 15)
$\Delta S_{k_{\text{ODH}}K_1}^\ddagger$ ^b	–254 (–200)	–261 (–207)	–259 (–175)	–255 (–171)	–177 (± 34)
$\Delta G_{k_{\text{ODH}}K_1}^\ddagger$ ^b	263 (243)	245 (225)	160 (129)	166 (135)	139 (± 21)
ΔE_{K_1} ^a		58	–48	–7	–
$\Delta(E+\text{ZPE})_{K_1}$ ^a		56	–45	–6	–
ΔH_{K_1} ^b		47 (53)	–69 (–47)	–17 (–7)	–23 (± 11)
ΔS_{K_1} ^b		–253 (–169)	–257 (–107)	–266 (–50)	–43 (± 25)
ΔG_{K_1} ^b		157 (126)	43 (–1)	98 (15)	–4 (± 15)

^aAt 0 K in vacuum. ^bDetermined for 433 K, 1 kPa. Values outside and inside parentheses reflect those calculated by removal of low-frequency vibrations and by their substitution with translations/rotations, respectively. ^cMeasured on $\text{H}_3\text{PMo}/\text{SiO}_2(0.16)$ at 20 kPa O_2 . Uncertainties reflect two times the standard deviations.

corresponding to a two-dimensional gas (two translational and three rotational degrees of freedom; entropy values for each mode are listed in Supporting Information, Table S.8). The TS corresponding to H-abstraction from this weakly adsorbed CH₃OH exhibited three low-frequency vibrations, which were treated as rotations, because translation becomes impossible as significantly strong O–H bonds form at the product-like transition state. Similarly, the strong H-bonded CH₃OH and its TS had four and three low-frequency modes, while methoxy species and their TS had three and two low-frequency modes, which were treated explicitly as translational and rotational degrees of freedom.

The enthalpies, entropies, and free energies for each adsorbate and TS in Table 2 show two values for each entry. The values outside parentheses were obtained by removing DFT-derived low-frequency modes, while those inside parentheses were obtained by replacing these modes with appropriate gaseous translations and rotations. The two values, therefore, reflect the minimum and maximum enthalpy and entropy estimates that can be obtained from different treatments of low-frequency modes. Enthalpy values did not change significantly with the removal or substitution of low frequencies with translation and rotation because these values depend significantly on DFT-derived ΔE values and zero-point energy contributions but not on thermal enthalpies derived from statistical mechanics using these vibrational frequencies (Table 2). Entropy values corresponding to first-order rate constants and CH₃OH adsorption equilibrium constants (between -254 and -267 J mol⁻¹ K⁻¹ for all cases, Table 2) obtained from the first approach are much smaller than values measured from temperature effects on rate and equilibrium constants (-177 ± 34 and -43 ± 25 J mol⁻¹ K⁻¹ for $k_{\text{ODH}}K_1$ and K_1 , respectively, Table 2) for all cases of intermediates and transition states examined. The inclusion of approximate values for translations and rotations gives entropy values for molecular routes (-171 and -50 J mol⁻¹ K⁻¹ for $k_{\text{ODH}}K_1$ and K_1 , respectively, Table 2) in reasonable agreement with measured values, but similar treatments for dissociative routes give entropies (-207 and -169 J mol⁻¹ K⁻¹ for $k_{\text{ODH}}K_1$ and K_1 , respectively, Table 2) that are more negative than measured values. These approximate corrections are not meant to bring entropies and free energies from theory and experiment into quantitative agreement, but they illustrate the significant entropies of weakly bound species and how sensitively they depend on the statistical mechanics methods used to estimate them. Among the different structures considered in Table 2 for each of the dissociative (D1-TSt1 and D1-Tsb3, Figure 3b) and molecular routes (M1-Tsb3 and M2-Tsb3, Figure 3b), the enthalpy and entropy values for the two transition states for each type of route have similar values; TS for both strong and weak H-bonded CH₃OH have similar agreement, while dissociative TS have similar lack of agreement, with experiments. In the case of adsorbed reactive species, however, the strong H-bonded CH₃OH (M2 species, Figure 3a) has entropy and enthalpy values lower than those of weak H-bonded CH₃OH; the latter values agree more closely with experiments (Table 2), suggesting that the protons may be covered with monomer species reactive for DME formation rates and that the prevalent molecular ODH route proceeds via the weakly bonded CH₃OH intermediates.

Figure 5 shows the values of first-order rate constants estimated from DFT-derived enthalpy and entropy contributions for molecular ($k_{\text{molec}}K_{1m}$; M1-Tsb3, Figure 3a, Table 2)

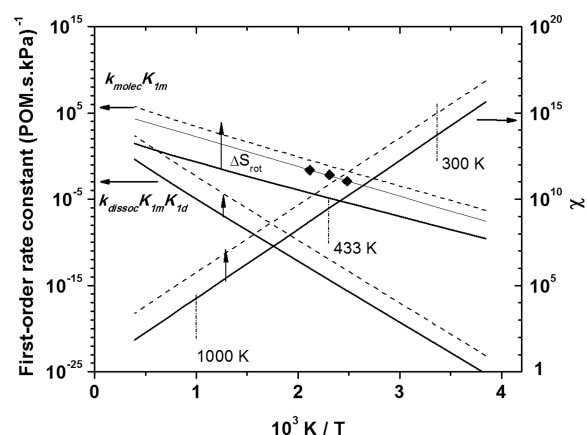


Figure 5. First-order rate constants from molecular ($k_{\text{molec}}K_{1m}$; Scheme 1) and dissociative ($k_{\text{dissoc}}K_{1m}K_{1d}$; Scheme 1) routes, the ratio of these rate constants (χ , eq 7) estimated from DFT-derived enthalpies and entropies on H₃PMo₁₂O₄₀ cluster, and measured rate constants (◆) on H₃PMo/SiO₂(0.16) (403, 433, and 473 K; 20 kPa O₂). Thick solid and dashed lines reflect the respective predicted values when enthalpic and entropic contributions from low-frequency vibrations were removed and when they were treated as rotational degrees of freedom equivalent to gas-phase molecules, respectively (values in Table 2).

and dissociative ($k_{\text{dissoc}}K_{1m}K_{1d}$; D1-TSt1, Figure 3b, Table 2) routes, as well as the ratio of these rate constants (χ from eq 7), and the measured rate constants as a function of reciprocal temperature. The enthalpy and entropy values obtained by removing low-frequency modes from vibrational partition functions lead to $k_{\text{molec}}K_{1m}$, $k_{\text{dissoc}}K_{1m}K_{1d}$, and χ values shown by solid lines (Figure 5). The rate constants for the dissociative route are much smaller than for the molecular route and depend more sensitively on temperature, consistent with its higher activation enthalpy. When the low-frequency vibrations were treated as rotations, the predicted rate constants increased without a significant change in their temperature dependence (slope), as a result of the different entropy estimates using these two methods (dashed lines in Figure 5). The O_M-atom in the molecular route TS is not bound to a Mo-atom of the POM cluster and have significant rotational freedom, which, when included in the entropy estimates, leads to increases in rate constants and the χ values. The measured rate constants lie within the bounds of predicted values using the two statistical mechanical treatments (solid and dashed lines) for molecular routes but are well-outside such bounds for dissociative route. The TS for the dissociative route has more positive enthalpies and more negative entropies than the TS structure that mediates molecular routes, making the molecular route much more facile based on both enthalpic and entropic factors (eq 8).

3.4. Influence of Theoretical Methods on Energetics of ODH Reaction Routes. DFT methods can lead to poor predictions of electronic band-gaps and reduction energies of periodic bulk oxides because of their inexact treatment of localized d-orbitals in transition metals.^{35,36} Hybrid-DFT functionals and DFT+U treatments^{35,36} are often used to ameliorate such inaccuracies. Here, we show that such inaccuracies are not significant for periodic plane-wave DFT calculations²⁹ on the nonperiodic POM clusters described above, thus confirming the mechanistic conclusions reached above using molecular basis set calculations³³ with DFT and hybrid-DFT functionals. We also estimate the effects of DFT +U and dispersion corrections to the periodic DFT calculations

described above. Detailed descriptions of these analyses are shown in the Supporting Information (section S.4); they indicate the following:

- (i) Molecular hybrid-DFT (B3LYP), which accurately predicts properties of other oxides,³⁵ and molecular DFT (PW91) methods gave similar energies for the addition of H-atom (HAE) to each O-atom in $\text{H}_3\text{PMo}_{12}\text{O}_{40}$ cluster, as periodic DFT (PW91-PAW) methods (within 15 kJ mol^{-1} among the three methods for various bridging and terminal O-atom). DFT+U methods (PW91-PAW, $U = 8.6$ as suggested for Mo in previous studies³⁶) give much more negative HAE values (70–140 kJ mol^{-1} more negative for various O-atoms) than the other treatments.
- (ii) Methoxy and molecularly adsorbed CH_3OH energies have similar values from periodic DFT (PW91-PAW), molecular hybrid-DFT (B3LYP), and periodic DFT+U (PW91-PAW, $U = 8.6$) calculations ($\Delta E_{\text{OH}/\text{OCH}_3^*} - \Delta E_{\text{CH}_3\text{OH}\cdot\text{O}^*} = 130, 136, \text{ and } 139 \text{ kJ mol}^{-1}$, respectively; Supporting Information, Table S.2), indicating that the steric effects discussed above are essentially independent of the method used.
- (iii) The TS energies for H-abstraction by $\text{O}_{\text{b}3}$ atom in the molecular route obtained using periodic DFT (PW91-PAW), molecular DFT (PW91), periodic DFT+U (PW91-PAW, $U = 8.6$) methods (70, 60, and -8 kJ mol^{-1} , respectively; Supporting Information, Table S.2) are consistent with significant underestimation of HAE by DFT+U and with similar energies for other methods (point (i) above). The TS with DFT+U method also gave early transition states with KIE values lower than experiments ($k_{\text{ODH}}K_1$ KIE values of 2.3 and 1.2 for DFT and DFT+U methods, respectively), suggesting that such methods with large U values (8.6) are unnecessary and inaccurate for POM clusters.
- (iv) Intermediates and transition states were treated as spin-polarized in DFT calculations, even for singlet structures, and their energies were compared with triplet and spin-restricted singlet states. For CH_2OH radicals in molecular routes, spin-polarized singlet states were the most stable configurations, consistent with diradical species,²⁴ which were confirmed using broken-symmetry molecular DFT (PW91) calculations (Supporting Information, Table S.3). Thus, our DFT treatments accurately detect such broken-symmetry structures when they prevail. All other structures involved in molecular and methoxy routes gave only symmetric (closed-shell) singlet configurations.
- (v) Inclusion of dispersion interactions using periodic vdWDF2-PAW methods⁴⁹ gave energies for molecularly adsorbed CH_3OH that differed by only $\sim 8 \text{ kJ mol}^{-1}$ from estimates using PW91-PAW methods, while TS energies differed by $\sim 6 \text{ kJ mol}^{-1}$ for these two methods, suggesting van der Waals effects are not very significant (Supporting Information, Table S.4).

We conclude from these extensive comparisons that the DFT methods used here accurately describe the redox energies of POM clusters, the potential energy surfaces for methanol ODH reactions, and the significantly different energies reported here for the transition states that mediate molecular and dissociative methanol ODH reaction routes.

3.5. H-atom Addition Energy as ODH Reactivity Descriptor and Probe of O-atom Properties.

Both molecular and dissociative CH_3OH ODH routes on $\text{H}_3\text{PMo}_{12}\text{O}_{40}$ clusters are mediated by H-abstraction transition states that occur late along the reaction coordinate, as evident from C–H bonds at the TS (Figure 3; $l_{\text{C-H}} = 0.138, 0.145, 0.144, 0.133, 0.141, \text{ and } 0.140 \text{ nm}$ for M1-TSb, M1-TSt, M2-TSb, D1-TS-b, D1-TSt, and D2-TSb, respectively) that are much longer than their respective adsorbed precursors (0.110 nm for molecular or methoxy structures) and O–H bonds (Figure 3; $l_{\text{O-H}} = 0.122, 0.116, 0.117, 0.131, 0.121, \text{ and } 0.120 \text{ nm}$, respectively) that resemble those in the product state (0.098–0.100 nm). Thus, the O–H bond energies in products, and therefore the energy of formation of O–H bonds from gaseous H-atoms, become the relevant descriptors of the H-abstrating ability of each O-atom in POM clusters and of ODH reactivity. The late nature of these TS structures is a common feature of both routes, even though molecular route TS have much lower energy than those for dissociative routes (70 kJ mol^{-1} vs 150 kJ mol^{-1} ; Figure 2) and prevail at conditions of ODH practice.

The known structure of Keggin polyoxometalate clusters, which allows accurate assessment of their catalytic properties, and rigorous comparisons between thermodynamics and kinetics from experiment and theory (Table 2, Figure 5) presented here can be used to propose descriptors of reactivity for oxides with more diverse compositions but known structures. A similar strategy led to predictive correlations between turnover rates and deprotonation energies for solid acids based on metal oxides.⁹

CH_3OH ODH on $\text{H}_3\text{PMo}_{12}\text{O}_{40}$ clusters proceeds via kinetically-relevant C–H bond breaking (in reactant) and O–H bond formation (at the catalyst surface) step that is mediated by a late TS. DFT calculations on other POM cluster compositions with Mo ($\text{H}_3\text{PMo}_{12}$, $\text{H}_4\text{SiMo}_{12}$) and W (H_3PW_{12}) addenda atoms and for partial substitution of Mo and W with V-atoms ($\text{H}_4\text{PV}_1\text{Mo}_{11}$, $\text{H}_4\text{PV}_1\text{W}_{10}$) show that the TS for molecular route was more stable than its dissociative counterpart (Figure 6a) on all compositions when the same O-atoms ($\text{O}_{\text{b}3}$; Supporting Information, Figure S.1; Figure 6c) were used to abstract H from CH_3OH , suggesting that the conclusions derived from $\text{H}_3\text{PMo}_{12}$ cluster remain valid over a wide range of composition and catalytic reactivity.

The energies of the TS for H-abstraction via molecular (M1-TSb or M1-TSt, Figure 3a) and dissociative (D2-TSb or D1-TSt, Figure 3b) routes were calculated at different bridging ($\text{O}_{\text{b}1}$ through $\text{O}_{\text{b}6}$, Figure 6c) and terminal ($\text{O}_{\text{t}1}$, Figure 6c) O-atoms on $\text{H}_3\text{PMo}_{12}$ clusters, and at one O-atom ($\text{O}_{\text{b}3}$) on $\text{H}_4\text{SiMo}_{12}$, H_3PW_{12} and two different isomers of $\text{H}_4\text{PV}_1\text{Mo}_{11}$, $\text{HPV}_1\text{W}_{10}$ clusters (shown in Figure 6c). Figure 6a shows these TS energies as a function of the H-atom addition energy at the same O-atom used for C–H bond activation. The H-atom addition energy is defined as the energy involved in adding a gaseous H-radical to a lattice O-atom in a metal oxide (e.g., $\text{H}_3\text{PMo}_{12}\text{O}_{40} + \text{H}^\bullet \rightarrow \text{H}_4\text{PMo}_{12}\text{O}_{40}$). This reaction forms OH bonds and transfers an electron to the catalyst, two processes that also occur in the formation of the H-abstraction transition state. The electrons and protons are accepted by the empty d-orbitals at metal centers and the O-atoms, respectively, even though the two are transferred simultaneously. Therefore, a more negative HAE reflects a more reducible metal center in the oxide catalyst or a more basic O-atom. The H-abstraction TS energies and HAE values vary with the location of the O-

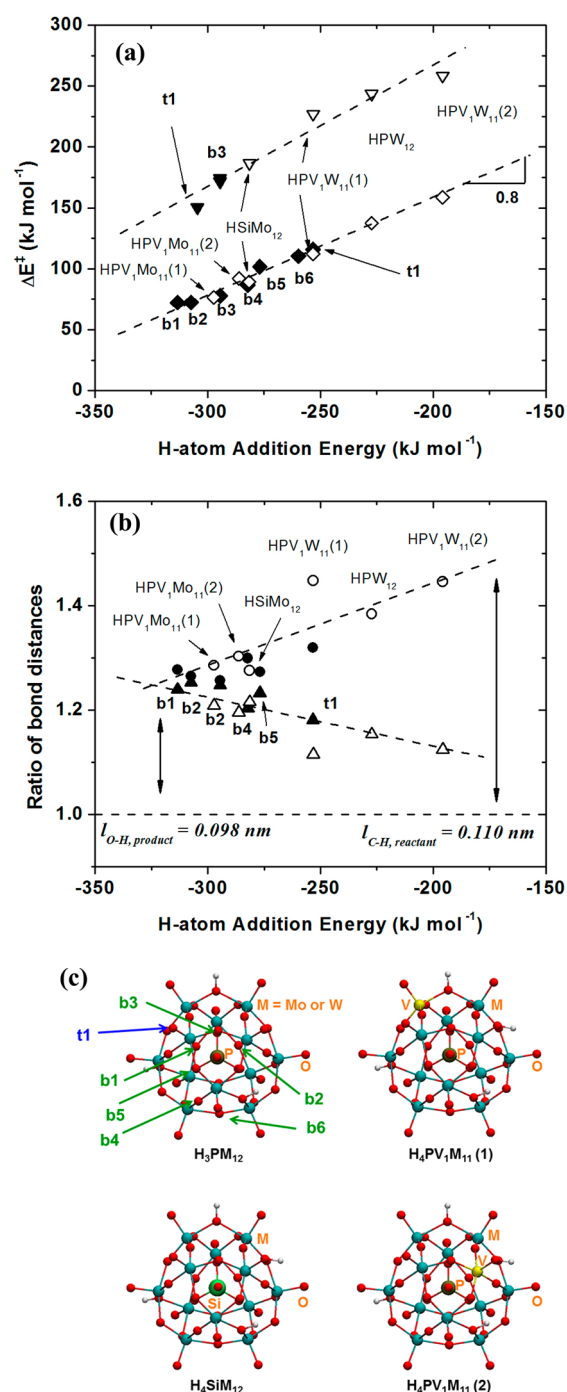


Figure 6. (a) DFT-derived energies of H-abstraction transition states (ΔE^\ddagger) for CH₃OH ODH via molecular (◆, ◇; M1-TSb and M1-TSt, Figure 3a) and dissociative (▼, ▽; D1-TSb, D2-TSb, and D1-TSt, Figure 3a) routes. (b) Ratios of C–H bond distances (●, ○) in TS to that in reactant CH₃OH molecule and of O–H bond distances (▲, △) in TS to that in product O_{POM}–H bond (for molecular TS only), calculated at different locations (O_{b1} through O_{b6} and O_{t1}, closed symbols) of O-atoms on a H₃PMo₁₂O₄₀ cluster and at O_{b3} atom on different POM compositions (open symbols) as a function of H-atom addition energies (HAE) of the O-atoms. (c) Locations of H-abstrating O-atoms on H₃PMo₁₂O₄₀ and the different POM compositions used to calculate ΔE^\ddagger and HAE values.

atom in a given POM cluster and with change in POM composition for a given location in each cluster. The TS energies for the molecular route, prevalent for ODH reaction

on POM clusters, are a single-valued and monotonic function of HAE for different bridging and terminal O-atom locations and for all compositions.

The energies for the molecular route TS structures on H₃PMo clusters were lower when bridging O-atoms (78 kJ mol⁻¹; M1-TSb3, Figure 3a) were used instead of terminal O-atoms (116 kJ mol⁻¹; M1-TSt1, Figure 3a), consistent with the more negative HAE value for the former (e.g., O_{b3} atom; Figure 6a). However, the dissociative route showed a TS energy for the terminal O-atom (150 kJ mol⁻¹; D1-TSt1, Figure 3a) lower than that for the bridging O-atom (171 kJ mol⁻¹; D1-TSb3, Figure 3a). These discrepancies reflect a decrease in the HAE value of the O_{t1} atom (–253 to –305 kJ mol⁻¹; Table 3), as a

Table 3. H-atom Addition Energies for Bridging (O_{b3}) and Terminal (O_{t1}) O-atoms of a Bare H₃PMo₁₂O₄₀ Cluster and a Cluster with Adsorbed Methoxy Species (Structure D1 in Figure 3b), Derived from Periodic DFT (PW91-PAW) Calculations

initial state of cluster	HAE values for different O-atoms (kJ mol ⁻¹)	
	O _{b3} atom	O _{t1} atom
bare cluster	–294	–253
adsorbed methoxy species	–296	–305

result of the presence of a methoxy group, but no significant change in its value for the O_{b3} atom (–294 to –296 kJ mol⁻¹; Table 3). Thus, dissociative route TS energies also show a single-valued correlation with HAE when the HAE values are calculated on clusters with methoxy species adsorbed near the abstracting O-atom (Figure 6a). The molecular routes prevail, however, under all practical reaction temperatures (Figure 5) and for all compositions (Figure 6a).

The lower TS energies of molecular routes compared to those of dissociative routes and their single-valued monotonic dependence on HAE suggest that HAE values represent accurate descriptors of methanol ODH reactivity. The slope of this dependence (Figure 6a) is close to unity (slope = 0.8), as expected for a very late transition state, whose stability reflects that of the product state. The “lateness” of the TS can be described by the C–H and O–H bond distances at the TS divided by their respective distances in the reactant C–H and the product O–H bonds. Figure 6b shows these ratios for molecular TS at O-atoms for different locations and composition as a function of HAE. The C–H bond becomes longer while the O–H bond becomes shorter for less negative HAE values, suggesting that the TS appears later along the reaction coordinate as the O–H bond in the product state becomes less stable with changes in location or composition. These results are consistent with Hammond’s postulate,⁵⁰ which indicates that the transition states for more endothermic reactions more closely resemble the product states than for less endothermic reactions. The linear relations between free energies of activation for ODH rate constants and HAE values, therefore, depend not only on the coefficient that reflects lateness of the TS but also on slight but monotonic changes in this coefficient with changes in HAE (Figure 6b).

HAE values reflect the energy of adding an electron and a proton (that make up the H-radical) to an oxidized POM cluster, which are accepted by the empty metal d-orbital and the O-atoms of the POM clusters, respectively. Its value can be described as a sum of the ionization energy of an H-atom (IE_{H} ,

independent of the cluster identity), the electron affinity of a neutral POM cluster (EA_{POM}), and the proton affinity of the reduced anion (PA_{Anion})

$$\text{HAE} = IE_{\text{H}} + EA_{\text{POM}} + PA_{\text{Anion}} \quad (9)$$

The EA_{POM} values reflect the energy of the lowest unoccupied molecular orbital (LUMO) set by the identity and coordination of the metal atoms. Alkane and alkanol ODH turnover rates (per metal atom) depend strongly on the identity of the addenda atom in the oxide and increase as the absorption edge energy in the ultraviolet (UV)–visible spectra of the oxide decreases.⁵¹ UV–visible edge energies reflect ligand-to-metal charge transfer events from the highest occupied molecular orbital (HOMO) in a lattice O-atom to the LUMO in a metal atom. Higher ODH turnover rates on oxides with smaller edge energies are consistent with H-abstraction transition states requiring electron transfer to the LUMO, which becomes more facile for lower LUMO energies. The HAE values (Figure 6a,b) for POM clusters with W addenda atoms are less negative than those with Mo addenda atoms, consistent with the larger UV–visible edge energies of W-POM clusters (Supporting Information, Figure S.4), which reflects their higher LUMO energies, because HOMO energies do not change significantly among these clusters.⁵²

The proton affinity (PA_{Anion} ; eq 9) of the anion formed after electron transfer reflects the basicity of the O-atom accepting the proton. Electron density maps derived from DFT calculations on $\text{H}_3\text{PMo}_{12}$ clusters (Supporting Information, Figure S.3) show that electrons are accepted by the same cluster Mo-atoms, suggesting that LUMO energies remain unchanged for all O-atom locations used for H-addition. Changes in HAE values with O-atom location instead reflect changes solely in the PA_{Anion} values. For $\text{H}_3\text{PMo}_{12}$ clusters, HAE values range from -313 to -260 kJ mol^{-1} at bridging O-atoms and -261 to -238 kJ mol^{-1} at terminal O-atoms; the less negative HAE of the latter type of O-atoms suggests that they are less basic and less reactive for ODH reactions.

The HAE values vary significantly with O-atom location on a POM cluster; therefore, a single HAE value cannot be used as a descriptor of its overall reactivity. For each cluster composition, ODH turnover rates reflect the reactivity-averaged HAE of all accessible O-atoms, which can be evaluated for each cluster composition to provide a rigorous and accurate predictor of oxidation reactivity for catalysts with known structure. Composition function relations developed from measured turnover rates and reactivity-averaged HAE on clusters with known structure, together with measurements of reactivity and UV–visible edge energies on oxides with uncertain structure (such as supported oxide-domains), can be used to estimate the effective HAE values of such oxides. The estimated HAE values and the measured UV–visible edge energies can then be used to infer plausible structures of active sites for oxide catalysts.

4. CONCLUSIONS

Mechanistic interpretations of CH_3OH ODH turnover rates on silica-supported Mo-based Keggin POM clusters ($\text{H}_3\text{PMo}_{12}\text{O}_{40}$) are compared with reaction pathways determined from theory. Kinetic and isotopic data are consistent with elementary steps based on Mars–van Krevelen redox cycles and with kinetically-relevant C–H bond activation step but cannot differentiate between H-abstraction from methoxy species and from CH_3OH molecule as the prevalent reaction route. Reaction pathways for both dissociative and molecular

routes determined from theory are consistent with the quasi-equilibrated and irreversible nature of elementary steps involved in ODH reaction, and they both yield predicted kinetic isotope effects ($\text{CD}_3\text{OD}/\text{CH}_3\text{OH}$ and $\text{CH}_3\text{OD}/\text{CH}_3\text{OH}$) consistent with measured values. The kinetically-relevant TS for the molecular route, however, has a much lower enthalpy and a higher entropy of activation than the dissociative route, suggesting that the former is overwhelmingly favored over the latter on POM clusters at all temperatures relevant to the practice of ODH catalysis. The octahedral coordination of Mo addenda atoms, also prevalent in most supported oxide domains of catalytic relevance, hinders the dissociative methanol insertion to form $\text{Mo}-\text{OCH}_3$ bonds leading to higher energies for dissociative routes.

The kinetically-relevant H-abstraction step proceeds via a product-like transition state, resulting in a strong dependence of TS energies on the strength of product O–H bonds. The TS energies for the molecular route prevalent on POM clusters change linearly with H-addition energy of the abstracting O-atom for different locations on $\text{HPMo}_{12}\text{O}_{40}$ cluster and for different POM compositions, suggesting that HAE is an accurate and complete descriptor of reactivity. HAE values probe the energetics of adding an electron to its unoccupied metal d-orbitals of clusters and a proton to the cluster O-atoms. The former is a global property of the clusters that depends on identity of the addenda atoms of the oxide, while the latter is sensitive to the type and location of O-atoms. As a result, HAE values vary with composition of the POM cluster as well as the location of O-atoms; accurate descriptors of reactivity require HAE values that are reactivity-averaged over all O-atom locations.

■ ASSOCIATED CONTENT

● Supporting Information

Primary and secondary reactions of $\text{CH}_3\text{OH}-\text{O}_2$ mixtures, derivation of CH_3OH ODH rate equations, atom positions on $\text{H}_3\text{PMo}_{12}\text{O}_{40}$ cluster, effects of different theoretical treatments on redox properties of POM clusters and energies of reactive species, structures and energies of different conformations of molecular and dissociative methanol adsorption and H-abstraction TS explored on $\text{H}_3\text{PMo}_{12}\text{O}_{40}$ clusters, calculations of enthalpies and entropies using statistical mechanics treatments, location of d-electron density introduced by H-atom addition to POM clusters, UV–visible absorption edge energies of POM clusters supported on SiO_2 . This material is available free of charge via the Internet at <http://pubs.acs.org>.

■ AUTHOR INFORMATION

Corresponding Author

*E-mail: iglesia@berkeley.edu.

Notes

The authors declare no competing financial interest.

■ ACKNOWLEDGMENTS

This material is based upon work supported by the U.S. Department of Energy, Office of Science, Office of Basic Energy Sciences, under contract DE-AC05-76RL0-1830. Computational facilities were provided by the Environmental Molecular Science Laboratory (EMSL) at Pacific Northwest National Laboratory (PNNL), a DOE Office of Science User Facility, under proposal 47582. The use of molecular DFT calculations using Gaussian program was made possible by the Extreme

Science and Engineering Discovery Environment (XSEDE) and a UC Berkeley College of Chemistry facility, which are supported by National Science Foundation grants (ACI-1053575 and CHE-0840505, respectively). We thank Dr. David Hibbitts (UC-Berkeley) for assistance with the statistical mechanics treatments and Dr. Robert Carr, Mr. William Knaeble, and Mr. Neelay Phadke (UC-Berkeley) for technical discussions and a critical review of the concepts developed in this manuscript.

REFERENCES

- (1) Pope, M. T.; Muller, A. Polyoxometalate Chemistry: An Old Field with New Dimensions in Several Disciplines. *Angew. Chem., Int. Ed.* **1991**, *30*, 34–48.
- (2) Okuhara, T.; Mizuno, N.; Misono, M. Catalytic Chemistry of Heteropoly Compounds. *Adv. Catal.* **1996**, *41*, 113–252.
- (3) Misono, M. Unique Acid Catalysis of Heteropoly Compounds (Heteropolyoxometalates) in the Solid State. *Chem. Commun. (Cambridge, U.K.)* **2001**, 1141–1152.
- (4) Song, I. K.; Barteau, M. A. Redox Properties of Keggin-type Heteropolyacid (HPA) Catalysts: Effect of Counter-Cation, Heteroatom, and Polyatom Substitution. *J. Mol. Catal. A: Chem.* **2004**, *212*, 229–236.
- (5) Barteau, M. A.; Lyons, J. E.; Song, I. K. Surface Chemistry and Catalysis on Well-Defined Oxide Surfaces: Nanoscale Design Bases for Single-Site Heterogeneous Catalysts. *J. Catal.* **2003**, *216*, 236–245.
- (6) Argyle, M. D.; Chen, K.; Bell, A. T.; Iglesia, E. Effect of Catalyst Structure on Oxidative Dehydrogenation of Ethane and Propane on Alumina-Supported Vanadia. *J. Catal.* **2002**, *208*, 139–149.
- (7) Liu, H.; Cheung, P.; Iglesia, E. Structure and Support Effects on the Selective Oxidation of Dimethylether to Formaldehyde Catalyzed by MoO_x Domains. *J. Catal.* **2003**, *217*, 222–232.
- (8) Liu, H.; Iglesia, E. Selective One-Step Synthesis of Dimethoxy-methane via Methanol or Dimethyl Ether Oxidation on $\text{H}^{3+n}\text{V}_n\text{Mo}_{12-n}\text{PO}_{40}$ Keggin Structures. *J. Phys. Chem. B* **2003**, *107*, 10840–10847.
- (9) Macht, J.; Carr, R. T.; Iglesia, E. Functional Assessment of the Strength of Solid Acids. *J. Catal.* **2009**, *264*, 54–66.
- (10) Schlögl, R. Concepts in Selective Oxidation of Small Alkane Molecules. In *Modern Heterogeneous Oxidation Catalysis: Design, Reactions and Characterization*; WILEY-VCH: Weinheim, Germany, 2009; p 1
- (11) Tatibouet, J. M. Methanol Oxidation as a Catalytic surface probe. *Appl. Catal., A* **1997**, *148*, 213–252.
- (12) Soares, A. P. V.; Portela, M. F.; Kiennemann, A. Methanol Selective Oxidation to Formaldehyde over Iron-Molybdate Catalysts. *Catal. Rev.* **2005**, *47*, 125–174.
- (13) Zhang, W.; Desikan, A.; Oyama, S. T. Effect of Support in Ethanol Oxidation on Molybdenum Oxide. *J. Phys. Chem.* **1995**, *99*, 14468–14476.
- (14) Seman, M.; Kondo, J. N.; Domen, K.; Radhakrishnan, R.; Oyama, S. T. Reactive and Inert Surface Species Observed during Methanol Oxidation over Silica-Supported Molybdenum Oxide. *J. Phys. Chem. B* **2002**, *106*, 12965–12977.
- (15) Kilos, B.; Bell, A. T.; Iglesia, E. Mechanism and Site Requirements for Ethanol Oxidation on Vanadium Oxide Domains. *J. Phys. Chem. C* **2009**, *113*, 2830–2836.
- (16) Liu, H.; Iglesia, E. Selective Oxidation of Methanol and Ethanol on Supported Ruthenium Oxide Clusters at Low Temperatures. *J. Phys. Chem. B* **2005**, *109*, 2155–2163.
- (17) Chen, K.; Khodakov, A.; Yang, J.; Bell, A. T.; Iglesia, E. Isotopic Tracer and Kinetic Studies of Oxidative Dehydrogenation Pathways on Vanadium Oxide Catalysts. *J. Catal.* **1999**, *186*, 325–333.
- (18) Mars, P.; van Krevelen, D. W. Oxidations Carried Out by Means of Vanadium Oxide Catalysts. *Chem. Eng. Sci.* **1954**, *3* (Supplement 1), 41–59.
- (19) Sojka, Z.; Che, M. EPR Study of the Interaction of O-ions with CH_3OH within the Coordination Sphere of Mo Ions Grafted on Silica: A New Approach for the Study of the Mechanism of Catalytic Reactions. *J. Phys. Chem.* **1995**, *99*, 5418–5430.
- (20) Gilardoni, F.; Bell, A. T.; Chakraborty, A.; Boulet, P. Density Functional Theory Calculations of the Oxidative Dehydrogenation of Propane on the (010) Surface of V_2O_5 . *J. Phys. Chem. B* **2000**, *104*, 12250–12255.
- (21) Hermann, K.; Michalak, A.; Witko, M. Cluster Model Studies on Oxygen Sites at the (010) Surfaces of V_2O_5 and MoO_3 . *Catal. Today* **1996**, *32*, 321–327.
- (22) Fu, H.; Liu, Z.; Li, Z.; Wang, W.; Fan, K. Periodic Density Functional Theory Study of Propane Oxidative Dehydrogenation over $\text{V}_2\text{O}_5(001)$ Surface. *J. Am. Chem. Soc.* **2006**, *128*, 11114–11123.
- (23) Jehng, J. M.; Hu, H.; Gao, X.; Wachs, I. E. The Dynamic States of Silica-supported Metal Oxide Catalysts during Methanol Oxidation. *Catal. Today* **1996**, *28*, 335–350.
- (24) Döbler, J.; Pritzsche, M.; Sauer, J. Oxidation of Methanol to Formaldehyde on Supported Vanadium Oxide Catalysts Compared to Gas Phase Molecules. *J. Am. Chem. Soc.* **2005**, *127*, 10861–10868.
- (25) Goodrow, A.; Bell, A. T. A Theoretical Investigation of the Selective Oxidation of Methanol to Formaldehyde on Isolated Vanadate Species Supported on Silica. *J. Phys. Chem. C* **2007**, *111*, 14753–14761.
- (26) Fievez, T.; Geerlings, P.; Weckhuysen, B. M.; Proft, F. D. Using DFT in Search for Support Effects During Methanol Oxidation on Supported Molybdenum Oxides. *ChemPhysChem* **2011**, *12*, 3281–3290.
- (27) Gregoriades, L. J.; Döbler, J.; Sauer, J. Oxidation of Methanol to Formaldehyde on Silica-Supported Molybdena: Density Functional Theory Study on Models of Mononuclear Sites. *J. Phys. Chem. C* **2010**, *114*, 2967–2979.
- (28) Rousseau, R.; Dixon, D. A.; Kay, B. D.; Dohnálek, Z. Dehydration, Dehydrogenation, and Condensation of Alcohols on Supported Oxide Catalysts Based on Cyclic $(\text{WO}_3)_3$ and $(\text{MoO}_3)_3$ Clusters. *Chem. Soc. Rev.* **2014**, *43*, 7664–7680.
- (29) Kresse, G.; Hafner, J. *Ab Initio* Molecular Dynamics for Liquid Metals. *Phys. Rev. B: Condens. Matter Mater. Phys.* **1993**, *47*, 558–561.
- (30) Kresse, G.; Furthmüller, J. Efficiency of *Ab-Initio* Total Energy Calculations for Metals and Semiconductors Using a Plane-wave Basis Set. *Comput. Mater. Sci.* **1996**, *6*, 15–50.
- (31) Perdew, J. P.; Chevary, J. A.; Vosko, S. H.; Jackson, K. A.; Pederson, M. R.; Singh, D. J.; Fiolhais, C. Atoms, Molecules, Solids, and Surfaces: Applications of the Generalized Gradient Approximation for Exchange and Correlation. *Phys. Rev. B: Condens. Matter Mater. Phys.* **1992**, *46*, 6671–6687.
- (32) Vanderbilt, D. Soft Self-consistent Pseudopotentials in a Generalized Eigenvalue Formalism. *Phys. Rev. B: Condens. Matter Mater. Phys.* **1990**, *41*, 7892–7895.
- (33) Frisch, M. J. et al. *Gaussian 09*; Gaussian, Inc.: Wallingford, CT, 2009.
- (34) Dudarev, S. L.; Manth, D. N.; Sutton, A. P. Effect of Mott-Hubbard Correlations on the Electronic Structure and Structural Stability of Uranium Dioxide. *Philos. Mag. B* **1997**, *75*, 613–628.
- (35) Paier, J.; Penschke, C.; Sauer, J. Oxygen Defects and Surface Chemistry of Ceria: Quantum Chemical Studies Compared to Experiment. *Chem. Rev. (Washington, DC, U.S.)* **2013**, *113*, 3949–3985.
- (36) Lutfalla, S.; Shapovalov, V.; Bell, A. T. Calibration of the DFT/GGA+ U Method for Determination of Reduction Energies for Transition and Rare Earth Metal Oxides of Ti, V, Mo, and Ce. *J. Chem. Theory Comput.* **2011**, *7*, 2218–2223.
- (37) Jónsson, H.; Mills, G.; Jacobsen, K. W. *Classical and Quantum Dynamics in Condensed Phase Simulations*; Berne, B.J., Ciccotti, G., Coker, D.F., Eds.; Kluwer Academic: New York, 1998; p 385.
- (38) Henkelman, G.; Jónsson, H. A Dimer Method for Finding Saddle Points on High Dimensional Potential Surfaces Using Only First Derivatives. *J. Chem. Phys.* **1999**, *111*, 7010–7022.
- (39) McQuarrie, D.A. *Statistical Mechanics*; University Science Books: Sausalito, CA, 2000.

- (40) Becke, A. D. Density-Functional Thermochemistry. III. The Role of Exact Exchange. *J. Chem. Phys.* **1993**, *98*, 5648–5652.
- (41) Lee, C.; Yang, W.; Parr, R. G. Development of the Colle-Salvetti Correlation-Energy Formula into a Functional of the Electron Density. *Phys. Rev. B: Condens. Matter Mater. Phys.* **1988**, *37*, 785–789.
- (42) Westheimer, F. H. The Magnitude of the Primary Kinetic Isotope Effect for Compounds of Hydrogen and Deuterium. *Chem. Rev. (Washington, DC, U.S.)* **1961**, *61*, 265–273.
- (43) Gounder, R.; Iglesia, E. The Roles of Entropy and Enthalpy in Stabilizing Ion-Pairs at Transition States in Zeolite Acid Catalysis. *Acc. Chem. Res.* **2012**, *45*, 229–238.
- (44) Rozanska, X.; Fortrie, R.; Sauer, J. Oxidative Dehydrogenation of Propane by Monomeric Vanadium Oxide Sites on Silica Support. *J. Phys. Chem. C* **2007**, *111*, 6041–6050.
- (45) Rozanska, X.; Sauer, J. Oxidative Dehydrogenation of Hydrocarbons by $V_3O_7^+$ Compared to Other Vanadium Oxide Species. *J. Phys. Chem. A* **2009**, *113*, 11586–11594.
- (46) Cheng, M. J.; Chenworth, K.; Oxgaard, J.; van Duin, A.; Goddard, W. A., III Single-site Vanadyl Activation, Functionalization, and Reoxidation Reaction Mechanism for Propane Oxidative Dehydrogenation on the Cubic V_4O_{10} Cluster. *J. Phys. Chem. C* **2007**, *111*, 5115–5127.
- (47) Sadakane, M.; Steckhan, E. Electrochemical Properties of Polyoxometalates as Electrocatalysts. *Chem. Rev. (Washington, DC, U.S.)* **1998**, *98*, 219–238.
- (48) Levy, R. M.; Karplus, M.; Kushick, J.; Perahia, D. Evaluation of the Configurational Entropy for Proteins: Application to Molecular Dynamics Simulations of an α -Helix. *Macromolecules* **1984**, *17*, 1370–1374.
- (49) Klimes, J.; Bowler, D. R.; Michelides, A. Chemical Accuracy for the van der Waals Density Functional. *J. Phys.: Condens. Matter* **2010**, *22*, 022201–1–5.
- (50) Hammond, G. S. A Correlation of Reaction Rates. *J. Am. Chem. Soc.* **1955**, *77*, 334–338.
- (51) Chen, K.; Bell, A. T.; Iglesia, E. The Relationship between the Electronic and Redox Properties of Dispersed Metal Oxides and Their Turnover Rates in Oxidative Dehydrogenation Reactions. *J. Catal.* **2002**, *209*, 35–42.
- (52) Weber, R. S. Molecular Orbital Study of C–H Bond Breaking during the Oxidative Dehydrogenation of Methanol Catalyzed by Metal Oxide Surfaces. *J. Phys. Chem.* **1994**, *98*, 2999–3005.